

5-2-2005

A Novel Valveless Micropump With Electrohydrodynamic Enhancement for High Heat Flux Cooling

Vishal Singhal

S V. Garimella

Purdue University, sureshg@purdue.edu

Follow this and additional works at: <http://docs.lib.purdue.edu/coolingpubs>

Singhal, Vishal and Garimella, S V., "A Novel Valveless Micropump With Electrohydrodynamic Enhancement for High Heat Flux Cooling" (2005). *CTRC Research Publications*. Paper 18.
<http://dx.doi.org/10.1109/TADVP.2005.847430>

This document has been made available through Purdue e-Pubs, a service of the Purdue University Libraries. Please contact epubs@purdue.edu for additional information.

A Novel Valveless Micropump with Electrohydrodynamic Enhancement for High Heat Flux Cooling¹

Vishal Singhal and Suresh V. Garimella²
School of Mechanical Engineering, Purdue University
West Lafayette, Indiana 47907-2088 USA

ABSTRACT

Integrated microchannel cooling systems, with micropumps integrated into microchannels, are an attractive alternative to stand-alone micropumps for liquid-cooled microchannel heat sinks. A new micropump design capable of integration into microchannels and especially suited for electronics cooling is presented. It combines induction electrohydrodynamics (EHD) with a valveless nozzle-diffuser micropump actuated using a vibrating diaphragm. A comprehensive numerical model of the micropump has been developed to study the combined effect of EHD and valveless micropumping. The numerical model has been validated using theoretical and experimental results from the literature. The flow rate achievable from the new micropump is presented and the effect of several key parameters on the micropump performance investigated.

¹ Submitted for publication in *IEEE Transactions on Advanced Packaging*, April 2004, and in revised form, October 2004

² To whom correspondence should be addressed: sureshg@ecn.purdue.edu; tel: (765) 494-5621; fax: (765) 494-0539

NOMENCLATURE

a	Diameter
A	Amplitude
D	Displacement vector
D_{IA}	Charge diffusion coefficient
E	Electric field
f	Frequency
F	Body force
h	Height
I_0	Modified Bessel's function of the first kind
J	Current density in the fluid
J_0	Bessel function of first kind
k	Wave number
l	Length
n	Width
q	Charge density in the fluid
r	Radial distance
Re	Reynolds number
s	Stress
$spac$	Spacing
t	Time
T	Temperature
v	Velocity
V	Voltage

w Displacement in z-direction

x x- coordinate

y y- coordinate

z z- coordinate

Subscripts and Superscripts

0 Initial

avg Average

c Center of pumping chamber

$elec$ Electrode

El Electric

io Inlet-outlet

nd Nozzle-diffuser

p Electric potential

vib Vibrating diaphragm

x x- direction

Greek Symbols

ϵ Permittivity of the fluid

θ Angle

λ Wavelength of the potential wave

μ Electrical mobility of the fluid

μ_{vis} Viscosity of the fluid

ρ Density of the fluid

σ Electrical conductivity of the fluid

$\Delta\sigma$ Difference in electrical conductivity

τ	Charge relaxation time
Φ	Potential
ω	Frequency

INTRODUCTION

Active liquid cooling with microchannels is an attractive solution for dissipating the ever-increasing heat loads from microprocessors and other electronic devices [1]. The pump used to force liquids through microchannels must be small, quiet, low-cost and reliable. For mobile applications, weight and power consumption of the pump are also issues of concern. Although several micropumps have been designed specifically for electronics cooling applications [2-4], none of them meet all the criteria mentioned above. A comprehensive review of these micropumps is provided in [5].

The work presented here is part of a larger research program to develop a low-cost integrated microchannel cooling system. A micropump integrated into microchannels eliminates the need for the extra space and weight of a separate micropump. Equally importantly, its fabrication can be integrated with that of the microchannels thus decreasing the overall cost of the cooling system. The design of a micropump suitable for integration into microchannels is the focus of the present work.

The design and working principle of the new micropump are first described. This is followed by a discussion of the two underlying technologies (valveless pumping and induction EHD), including a review of the literature and theoretical analysis for each. The numerical modeling approach used to predict the performance of the pump is then presented, along with validation results. Results from the model are then presented and discussed to illustrate the working and advantages of the pump.

WORKING PRINCIPLE OF THE MICROPUMP

The new micropump integrates two existing pumping technologies. It consists of a valveless nozzle-diffuser pump with a series of thin, closely spaced parallel electrodes deposited in the nozzle-diffuser elements, as schematically shown in Figure 1. The two nozzle-diffuser elements are connected through a pumping chamber. A (piezoelectrically actuated) diaphragm drives the fluid in the pumping chamber. Electrodes deposited in the nozzle-diffuser elements are connected to a single- or poly-phase power supply, which, together with the diaphragm operation, drives the flow.

Actuating the diaphragm causes a continual, periodic increase and decrease in the volume of the pumping chamber (Figure 2). When the volume of the pumping chamber increases, the pressure in the chamber decreases and more fluid enters through the nozzle-diffuser element on the right (inlet) relative to that on the left (outlet). This is because the element on the right acts as a diffuser, which poses less flow resistance than the nozzle on the left. Conversely when the volume of the pumping chamber decreases, more fluid exits through the element on the left, which now acts as a diffuser. This results in a net pumping action from right to left in Figure 2, as the diaphragm vibrates up and down.

Actuating the electrodes leads to further pumping action due to induction of charges and the resultant Coulomb forces generated in the fluid. When the microelectronic component being cooled is operational, the fluid present in the microchannel experiences a temperature gradient across the height of the channel. This temperature gradient in turn causes a gradient in the electrical conductivity of the fluid. When an alternating voltage is applied to the electrodes, a traveling electric field propagates through the working fluid in the nozzle-diffuser elements. The traveling field results in an induction of charges in bulk of the fluid. These charges are displaced

due to charge relaxation and hence interact with the traveling wave, which leads to the application of Coulomb forces on the charges. These moving charges carry bulk fluid with them due to viscous effects, and this leads to a pumping action. This process is generally known as induction electrohydrodynamics (EHD), a more detailed explanation of which is provided below.

The combined operation of the vibrating diaphragm and induction EHD can lead to significantly higher flow rates relative to their operation independent of each other. This is the central idea of the new micropump presented in this work.

VALVELESS NOZZLE-DIFFUSER MICROPUMP

Several different designs of valveless micropumps employing fixed valves have been proposed in the literature [6-8]. The key enabling feature of these pumps is the flow rectification caused by the differing flow and pressure drop characteristics of fixed valves for flow in opposite directions. Nozzle-diffuser elements (either spatial [6, 7] or planar [9]) are the most widely used type of fixed valves in micropumps, which may be actuated by piezoelectric [6,7], electromagnetic [9], or thermopneumatic [10] means. Pumps with two diaphragms operating in opposite phases have also been considered [11,12]. Several efforts have been made to optimize the nozzle-diffuser elements to increase the flow rate of such pumps [13,14]. A detailed review of valveless nozzle-diffuser micropumps is available in [5].

Nozzle-diffuser micropumps can achieve higher flow rates than many other micropumps [5]; Olsson et al. [12] reported a flow rate of 3.5 ml/min for a nozzle-diffuser micropump of dimensions 15×17×1.4 mm. Flow rates that are higher by several orders of magnitude are possible in spite of the imperfect flow rectification properties of such valves, since these micropumps can be operated at much higher frequencies (~10 kHz) than those with passive check valves (a few hundred Hz). Moreover, when excited to the resonance frequency of the

system, the efficiency (flow rate for a given power input) achievable with such pumps can be large.

The ability of a valveless micropump to direct flow in a preferential direction can be expressed in terms of flow rectification efficiency ε , as $\varepsilon = (Q_+ - Q_-)/(Q_+ + Q_-)$ where Q_+ and Q_- are the volumes of fluid moving through a nozzle-diffuser element in the diffuser and the nozzle directions, respectively, during one pumping cycle. When $\varepsilon = 0$, there is no rectification (no net flow) while $\varepsilon = 1$ implies perfect rectification. For a given design of the actuation unit, the pump flow rate will depend on ε . Typical values of ε in the range of 0.01 – 0.05 have been reported for such pumps [13].

The motion of the vibrating diaphragm in a pump gives rise to a pressure gradient between the pumping chamber and the inlet/outlet chambers. When the diaphragm moves outwards, the volume of the pumping chamber increases and its pressure decreases, and conversely. Both the amplitude and frequency of diaphragm vibration determine this change in pressure. While the fluid-diaphragm interaction can also affect pressure, this effect is neglected in the present analysis.

The diaphragm vibration was modeled using the mode shape for the first mode of vibration of a circular plate with a simply supported edge. It is given by

$$w_{vib}(r, t) = A \left[J_0 \left(\frac{\lambda r}{a/2} \right) - \frac{J_0(\lambda)}{I_0(\lambda)} I_0 \left(\frac{\lambda r}{a/2} \right) \right] \sin(\omega t) \quad (1)$$

In the above equation, $\lambda = 2.231$ for the first mode of vibration, and w_{vib} represents the orthogonal displacement of the diaphragm at a distance r from the center of the plate at time t .

The velocity of the plate is obtained by differentiating Eq. (1) with respect to time:

$$v_{vib}(r, t) = \omega A \left[J_0 \left(\frac{\lambda r}{a/2} \right) - \frac{J_0(\lambda)}{I_0(\lambda)} I_0 \left(\frac{\lambda r}{a/2} \right) \right] \cos(\omega t) \quad (2)$$

The action of the vibrating diaphragm was included in the numerical model solely by specifying its motion, i.e., its position and velocity at different radial distances with time, according to Eqs. (1) and (2), respectively.

INDUCTION EHD

EHD refers to the mutual effects of fluid motion, charges in the fluid and the electric field on one another. Pumping of fluids using EHD has long been investigated in the literature [15,16]. EHD pumps directly convert electrical energy into fluid motion. Most EHD pumps use an electric field to pull along ions because of Coulomb forces, which in turn drag the bulk fluid by momentum transfer due to fluid viscosity. Therefore, EHD pumping requires: a) the presence of free charges in the fluid, and b) an electric field to move these charges.

In most EHD pumps, charges (ions, or electrons which combine with neutral molecules to form ions) are either injected into the fluid [17-19] or regions of high charge density are created due to the presence of charges on the surface [20,21]. The pumps based on these two phenomena are called injection EHD (or ion-drag) pumps and electro-osmotic pumps, respectively.

Charges can also be induced into a fluid [22,23] (induction EHD), by a dissociation of neutral molecules into positively and negatively charged ions [24,25]. The net charge, averaged over the entire fluid, is zero in this case whereas it is non-zero for both injection EHD and electro-osmotic pumping. Induction of charges can only be caused in a fluid with a spatial variation – either a continuous gradient or sudden jumps – in electrical conductivity or permittivity. Significant gradients in electrical conductivity can be obtained in several dielectric and some polar liquids by anisotropic heating or cooling of these liquids [23], as their electrical conductivity is a function of temperature. Jumps in electrical permittivity and electrical

conductivity can be obtained through the use of layers of non-mixing fluids [22] or suspended particles or bubbles [26] in the fluid.

Induction of charges also requires a traveling potential wave, moving perpendicular to the direction of variation in electrical conductivity or permittivity. The traveling electric field is commonly generated by a series of parallel electrodes connected to a single- or poly-phase power supply.

Induction EHD in flow between parallel plates is illustrated in Figure 3a, with the lower plate heated and the upper plate cooled. The potential field is applied using electrodes located along the length of the upper plate. If the fluid electrical conductivity is dependent on temperature, a conductivity gradient would be established in the distance between the plates, with the fluid close to the lower plate having the highest conductivity corresponding to the highest temperature. A traveling electrical wave along the length of the upper plate would cause a dissociation of molecules in the region of high conductivity and high electric field. The electrical conductivity is lowest close to the upper plate, while the electric field decreases with distance away from it. Hence the free charges are created slightly away from the upper plate, where both electrical conductivity and electric field are relatively high. Positive and negative charges thus created are attracted towards the electrodes of opposite polarity along the top surface, and tend to move towards these electrodes. However, this movement becomes progressively slower because the electrical conductivity is smaller close to the cold wall [25]. This leads to the formation of alternating bands of positive and negative ions in the fluid. These charges react to the movement of the potential field, by being attracted to the closest electrode, and hence move in the same direction as the potential wave, but lag behind the traveling wave in phase. This mode is often referred to as attraction-type induction EHD pumping. In such

pumps, the maximum velocity of the fluid can not exceed the speed of the potential wave, which is given by $v = \lambda_p \cdot f_p$. This is known as the synchronous speed of the pump.

If, on the other hand, the electrodes are located along the lower plate, the dissociation of neutral molecules into positive and negative charges takes place very close to this plate as both electrical conductivity and electric field are highest close to this plate, as shown in Figure 3b. In this case, like charges are repelled by the electrodes away from the plate, while unlike charges collect on the electrodes [25]. As the potential wave travels, the charges are repelled by the nearest electrode, which leads to their motion in the direction opposite to that of the potential wave. This is known as repulsion-type induction EHD pumping. There is no limiting speed in this mode of operation.

In the case of a pump with layers of non-mixing fluids or the presence of bubbles in the liquid, the induced charges relax to the boundary between homogeneous components. These charges move either in the same or in the opposite direction as the potential wave depending on the relative conductivity of the fluid closer to electrodes (opposite direction if higher, same direction if lower). If there are no conductivity or permittivity gradients in the bulk of the fluid, there would not be any free charges in the bulk.

The charges in an induction EHD pump tend to neutralize in a time period of the order of the charge relaxation time τ , $\tau = \epsilon/\sigma$. Additional charges are induced (created) to make up for loss of these charges. Since the charge relaxation time is of the order of milliseconds or even smaller for most liquids, the *life* of induced charges is generally much smaller than the time required for charges to move from one electrode to next. However, in cases where the charge relaxation time is relatively large, such as for insulating oils, and when the electrode spacing is small, charge clouds can move from one electrode to another before being neutralized.

Irrespective of the charge relaxation time, charges are continually induced and neutralized in the same charge cloud.

Early work on macroscale induction-type EHD pumps was based both on abrupt jumps [22] and on smooth gradients in electrical conductivity of fluids [23]. A theoretical model based on the charge density approach was used to predict the pump performance. Gerdt et al. [27] investigated the use of induction EHD to pump cooling oil in underground electric power cables, for which a numerical model was presented in [28]. Theoretical and experimental studies on a vertical induction EHD pump were reported in [25,29]. The model presented in [25] was used to study the pumping potential of an induction EHD pump in space [30]. The optimal frequency for maximizing the flow rate was calculated analytically in [31]; the results agreed with the experiments reported in [29]. The effect of charge relaxation time, fluid conductivity and fluid layer thicknesses on efficiency of attraction-type EHD induction pumps based on electrical conductivity jump at the interface of two fluid layers was reported in [32].

Microscale induction EHD pumps have also been investigated for different applications [33-37]. The performance of various fluids, with and without antistatic dopants, in induction EHD has been considered [38]. Heat transfer enhancement obtained through induction EHD pumping, especially that caused by a temperature gradient due to heated/cooled walls, has also received attention [39-41]. The pumping action due to induction of charges at the interface between a liquid and a gas has also been investigated [26,42,43].

Theoretical Analysis

Governing equations developed for EHD are briefly discussed here under the assumption that moving electric charges cause negligible magnetic induction, and are discussed in greater detail in [44].

The electric field E (V/m), can be related to potential Φ (V), using

$$\vec{E} = -\vec{\nabla}\Phi \quad (3)$$

The free charge density q (C/m³), in the fluid is given by

$$q = \vec{\nabla} \cdot \vec{D} \quad (4)$$

where D (C/m²) is the displacement vector, which for most liquids and gases is given by

$$\vec{D} = \epsilon\vec{E} \quad (5)$$

The current density J , is given by

$$\vec{J} = \sigma\vec{E} + q\mu\vec{E} + q\vec{v} - D_{IA}\vec{\nabla}q \quad (6)$$

The four terms on the right hand side of Eq. (6) represent, in order, currents due to conduction, ionic mobility, convection and diffusion of charges; detailed explanations are available in [44,45]. Equations (3), (4) and (5) can be combined into Poisson's equation, which relates the electric potential to the charge density as

$$q = -\vec{\nabla} \cdot (\epsilon\vec{\nabla}\Phi) \quad (7)$$

Since charge density in the fluid is not known *a priori*, this equation cannot be solved independently. However, if the charge density in the fluid is too small to affect the potential field significantly and the permittivity is constant, Eq. (7) reduces to the Laplace equation, $\nabla^2\Phi = 0$, which can be solved if appropriate boundary conditions are supplied.

The current density is related to the free charge density as

$$\vec{\nabla} \cdot \vec{J} + \partial q / \partial t = 0 \quad (8)$$

The unsteady charge transport equation can be written by combining Eqs. (6) and (8) as

$$\partial q / \partial t + \vec{\nabla} \cdot (q\vec{v}) = \vec{\nabla} \cdot (\sigma\vec{\nabla}\Phi + q\mu\vec{\nabla}\Phi + D_{IA}\vec{\nabla}q) \quad (9)$$

All the variable vectors and scalars in Eqs. (3)-(9) are functions of x , y , z and t . In addition, σ is a function of the electric field and charge density in the fluid. Assuming that local and temporal variation of ϵ and σ are known, there are six variables in this set of equations: Φ ,

\vec{E} , \vec{D} , q , \vec{J} , \vec{v} . This set of equations can be solved along with the Navier-Stokes equations below (modified to include an extra term because of Coulomb forces (Eq. (11)), to determine the potential and charge distribution and the flow field:

$$\text{Continuity:} \quad \frac{\partial \rho}{\partial t} + \vec{\nabla} \cdot \rho \vec{v} = 0 \quad (10)$$

$$\text{Navier-Stokes:} \quad \frac{\partial \rho \vec{v}}{\partial t} + (\vec{v} \cdot \vec{\nabla}) \vec{v} = -\vec{\nabla} p + \vec{\nabla} \cdot s_{ij} + \rho \vec{F} - q \vec{\nabla} \Phi \quad (11)$$

Under the assumptions of negligible charge transport due to diffusion (true for most liquids) and that due to convection and ion mobility, Eqs. (7) and (9) reduce to:

$$\frac{\partial q}{\partial t} + \frac{\sigma}{\epsilon} q = \vec{\nabla} \sigma \cdot \vec{\nabla} \Phi - \frac{\sigma}{\epsilon} \vec{\nabla} \epsilon \cdot \vec{\nabla} \Phi \quad (12)$$

If there is no spatial gradient of potential and no spatial variation in electrical conductivity or permittivity, Eq. (12) reduces further to

$$\frac{\partial q}{\partial t} + \frac{\sigma}{\epsilon} q = 0 \quad (13)$$

The solution of this equation is $q = q_0 e^{-(\sigma/\epsilon)t}$, where q_0 is the initial charge density.

Therefore, any charge present in the fluid would decay in a time of the order of the charge relaxation time (ϵ/σ). If, on the other hand, a spatial variation of the potential field and a gradient in electric conductivity or permittivity exist, there would be a non-zero term on the right hand side in Eq. (13), which would necessitate a non-zero charge density in the fluid at all times.

Assuming that the right hand side of Eq. (12) does not vary significantly with time, its solution

can be written as $q = \frac{\epsilon}{\sigma} C + \left(q_0 - \frac{\epsilon}{\sigma} C \right) e^{-(\sigma/\epsilon)t}$, where $C = \vec{\nabla} \sigma \cdot \vec{\nabla} \Phi - \frac{\sigma}{\epsilon} \vec{\nabla} \epsilon \cdot \vec{\nabla} \Phi$. Here, a

component of charge density given by $\frac{\epsilon}{\sigma} \vec{\nabla} \sigma \cdot \vec{\nabla} \Phi - \vec{\nabla} \epsilon \cdot \vec{\nabla} \Phi$ would not decay with time, as long

as the potential gradient and conductivity or permittivity variation are present. Also, even in the

absence of initial free charges in the fluid, charge induction would occur, which would cause dissociation of neutral molecules into positive and negative ions to satisfy Eq. (12).

NUMERICAL MODELING OF MICROPUMP

The commercially available computational fluid dynamics software package, FIDAP [46], was adapted for use in the numerical modeling. This package uses finite elements for the discretization of differential equations. A built-in EHD module was used for modeling induction EHD. This was accomplished by introducing additional species equations to solve for the voltage and charge density distributions. The vibrating diaphragm was modeled by specifying its position and speed as a function of time. The effect of fluid-structure interaction on the diaphragm motion was neglected. Remeshing due to motion of the free-surface was handled using a “spines” approach: The free-surface nodes and a specified number of nodes in a line below this node move along fixed specified curves, called spines. User-defined subroutines were used for applying boundary conditions for modeling EHD and the vibrating diaphragm.

The pump geometry modeled is shown in Figure 4. Since the geometry of the pump is symmetrical, only a half of the pump was modeled. The top view of half of a stand-alone pump (not integrated into microchannels) is shown in Figure 4a. The axis of symmetry is shown with a dotted line. An isometric view of the pump, with side walls shaded, is shown in Figure 4b. The electrodes which lie along the bottom and side-walls of the nozzle-diffuser elements are not shown. The geometry of the pump, as shown in Figure 4 with a uniform depth of h (not shown in the figure), was constructed using GAMBIT [47]. The nozzle-diffuser elements were meshed with a uniform mesh along their length, while a graded mesh was used in the other directions. This was necessary because the electrodes are modeled dynamically with a user-subroutine. Uniform meshing ensures that each electrode is represented by an equal number of finite

elements since all electrodes have the same width. A mesh with eight elements along the width of the nozzle-diffuser elements and 25 along their length is shown on the bottom surface of the pump in Figure 4b. Here, each electrode is represented by one element in the mesh. In finer meshes used for mesh-independence studies, each electrode was represented by up to 4 elements.

Vibrating Diaphragm Model Validation

The numerical model for the vibrating diaphragm was validated by simulating the nozzle-diffuser micropump of Kim and Xu [48]. The pump consisted of a pumping chamber of diameter 6 mm. The nozzle-diffuser elements were 2.32 mm long and 45 μm wide at the neck. The half-angle of the nozzle-diffuser elements was 4.9°. The depth of the pump was 120 μm . The pump, fabricated using laser micromachining, was electromagnetically actuated. The experiments were performed with deionized water as the working fluid and results were reported in terms of maximum flow rate (obtained at zero pressure head).

Results from a numerical model of the pump using the commercial computational fluid dynamics software, FLUENT [49], were also reported in [48]. The diaphragm was assumed to move in a sinusoidal fashion and its motion was simulated using:

$$z_{vib}(r,t) = A \cos(\pi r/a) \sin(\omega t) \quad (14)$$

Although the pump included inlet and outlet chambers, these were not included in the model in [48]. Their experimental and numerical results for average flow rate, at a diaphragm amplitude of 6 μm and frequency 1 Hz, are shown in Table 1. The numerical predictions in [48] for flow rate were approximately three times higher than the experimental values. Kim and Xu attributed this difference to: a) back pressure from the inlet and outlet chambers, b) surface roughness arising from laser micro machining, and c) bubbles trapped in the pump due to cavitation.

The pump geometry in [48] was simulated using the present model. Two alternative representations were studied, one without and the other with the inlet and outlet chambers

included. The first case corresponds to the numerical model of [48], while the second more closely simulates the experimental situation. The average flow rates obtained from the present simulations are also listed in Table 1. With the inlet and outlet chambers not included, the present results match the numerical results for average flow rate in [48]. However, with these chambers included in the model, the average flow rate obtained with the present model was much smaller, agreeing more closely with the experimental measurements.

EHD Model Validation

The EHD model in the present work was validated in two steps: in the first, only the transport of electric charge was considered (as reported in [44]), while in the second validation presented here, both induction and transport of charges are included.

Charge induction is modeled for fully developed flow in the parallel plates geometry shown in Figure 5a. The plates are maintained at different constant temperatures, causing an almost linear temperature distribution in the fluid region between the plates, which is assumed to result in a linear electrical conductivity gradient. The plate at the lower temperature is maintained at zero potential while a traveling sinusoidal potential wave is applied to the one at the higher temperature. Because of the electrical conductivity gradient, the traveling electric wave causes induction of charges in the bulk fluid. Coulomb forces on these charges due to the electric field lead to motion of the bulk fluid. An analytical solution for this problem [23] is used as the basis for validation of the present numerical analysis.

The analytical solution in [23] involves additional assumptions than those already discussed. The permittivity of the fluid is assumed to be a constant. Only the contribution of charge conduction to the current density (electrical conductivity of the fluid) was considered in the analysis; contributions from charge mobility and charge convection were neglected. This is a fairly good assumption for flows with small Re_{EI} ($Re_{EI} < 0.1$). $Re_{EI} = \epsilon v / \sigma l$ is the Electric

Reynolds number. It is the ratio of the free charge relaxation time of the fluid (ε/σ) to the time which characterizes system dynamics (l/v), and also reflects the efficiency of energy conversion. Even though the flow is transient, it was assumed to be quasi-static and a time-averaged analysis was performed. The variation of electric potential at any depth with distance along the length of the pump and time was assumed to be the same as that of the potential wave applied at the wall held at the higher temperature, *i.e.*, the x and t dependence of the potential wave at all y had the same form as the applied potential. A few other assumptions, regarding the electrical conductivity gradient, were made to simplify the partial differential equations to achieve the following analytical solution:

$$v_x = Dd \left[F \int_0^{\zeta} \frac{d\zeta}{\mu(\zeta)} - \int_0^{\zeta} \frac{f(\zeta)}{\mu(\zeta)} d\zeta \right]$$

In equation (15), $D = \varepsilon k \hat{V} \hat{V}^* / [4d(\cosh b_r - \cos b_i)]$, $F = \int_0^1 \frac{f(\zeta)}{\mu(\zeta)} d\zeta / \int_0^1 \frac{d\zeta}{\mu(\zeta)}$, and

$$f(\zeta) = e^{-a_r(\zeta-1)} [b_r \sin(b_i \zeta) - b_i \sinh(b_r \zeta) + a_i (\cosh(b_r \zeta) - \cos(b_i \zeta))].$$
 Here, $\zeta = y/d$ is the

nondimensional distance from the plate at the lower temperature, d is the absolute distance between the plates, $a_r = \eta / (1 + S^2)$, $a_i = -\eta S / (1 + S^2)$, $b_r = A \cos(\theta/2)$ and $b_i = -A \sin(\theta/2)$.

In the expressions for b_r and b_i , $A = \left\{ \left[4(kd)^2 + \eta^2(1 - S^2) / (1 + S^2)^2 \right]^2 + \left[2\eta^2 S / (1 + S^2)^2 \right]^2 \right\}^{1/4}$,

and $\theta = \tan^{-1} \left\{ \left[2\eta^2 S / (1 + S^2)^2 \right] / \left[4(kd)^2 + \eta^2(1 - S^2) / (1 + S^2)^2 \right] \right\}$. Here, $k = 2\pi/\lambda$ is wave

number, $\eta = \Delta\sigma / \sigma_{avg}$ is the ratio of the electrical conductivity difference between top and

bottom plates to the average electrical conductivity of the fluid between the plates, and

$S = \omega\varepsilon / \sigma_{avg}$ is a nondimensional parameter which can be thought of as a different electric

Reynolds number for traveling wave-type EHD, where the characteristic time represents wave

dynamics, instead of system dynamics (period of the potential wave is $2\pi/\omega$). This number has special significance because the bulk fluid velocity with induction-EHD reaches a maximum when $S = 1$, *i.e.*, when $f = \sigma_{avg}/(2\pi\epsilon)$.

A pump with the following parameters was simulated using the present model: distance between parallel plates $d = 5$ mm, fluid viscosity $\mu = 1$ Ns/m², permittivity $\epsilon = 1.0 \times 10^{-6}$ F/m and electrical conductivity variation from 0.995×10^{-6} S/m to 1.005×10^{-6} S/m ($\therefore \eta = 0.01$). The voltage amplitude, frequency and wavelength of the potential wave were $V = 10$ kV, $f = 1$ Hz and $\lambda = 0.625$ m, respectively. Hence the electrical Reynolds number, $Re_{EI} = (\epsilon/\sigma)/(l/v) = 0.05$. The characteristic velocity v is the average velocity in the channel and characteristic length l is the wavelength of the potential wave. This is similar to the cases described in [23,27,28] in terms of both pump dimensions and fluid properties.

Results for time-averaged fluid velocity in the channel, obtained from the analytical solution of [23] and from the present numerical model, are compared in Figure 5b. The flow caused is in a direction opposite to that of the potential wave because the electric potential is higher in the fluid of higher conductivity. The analytical and numerical results match closely.

Melcher and Firebaugh [23] used the electric shear stress approach, instead of the force density approach, to calculate the flow profile due to induction EHD. Use of the electric shear stress approach enabled them to neglect the time and space-variation in induced charge density and to assume the flow to be quasi-static. Hence the resultant Navier-Stokes equations were time-independent and one-dimensional, making them amenable to analytical solution. Seyed-Yagoobi et al. [25] followed a similar approach but considered developing flow as well. In the present work, the force density approach has been used for the first time to successfully model induction EHD. The model can predict the induced charge density as a function of both space and time. The present model also predicts flow transients due to induction EHD, which has not

been accounted for in any previous model. Moreover, the effect of different voltage profiles, as well as of the presence of separate electrodes, can be considered in the present model. These capabilities of the model are demonstrated in [44].

RESULTS AND DISCUSSION

The model domain shown in Figure 3 is considered in the analysis, with pump dimensions as given in Table 2. Water, doped with potassium chloride to increase its electrical conductivity gradient with temperature, was used as the working fluid, with properties as listed in Table 3. The electrical properties are obtained from [35] while the thermomechanical properties are those of pure water evaluated at the average fluid temperature of 50°C [50]. A temperature difference of 5°C is assumed between the top and bottom walls of the pump, with the bottom wall being at the higher temperature. The electrical conductivity varies linearly with temperature [35]. The operation of the new micropump proposed here is studied for three different cases consisting of two different vibrating diaphragm diameters (1 and 2 mm) and two different electrode widths (10 and 5 μm each); the width of the electrodes is the same as their spacing. A six-phase power supply with phases being 60 deg apart from each other was considered. Every sixth electrode was connected to a given phase of this power supply. The frequency of the potential wave was 122 kHz, which is the optimal frequency for achieving maximum flow rate due to EHD alone for the present fluid [23,31]. Values of other parameters of the pump are given in Table 2.

Mesh-Independence

The flow rate at zero back pressure achieved from EHD action only for the pump with $a_c = 1$ mm and $n_{elec} = spac_{elec} = 10$ μm is plotted in Figure 6a for three different meshes, with results for larger times shown in Figure 6b. The flow rate is plotted as a function of time, where time t

= 0 corresponds to a stationary state with zero fluid velocity, no electric field and no free charges anywhere in the fluid. The electric potential is applied at $t = 0$, which leads to induction of charges and bulk fluid motion.

Mesh 1, shown in Figure 4b, has 8 elements along the width of the nozzle-diffuser elements, 25 elements along their length, 28 elements along the width of the inlet and outlet chambers, 18 elements along their length, 21 elements at the widest point of the pumping chamber and 60 along its length. There are 8 elements along the pump height. Mesh 2 is approximately eight ($2 \times 2 \times 2$) times finer than Mesh 1, *i.e.*, it has twice the number of elements as Mesh 1 in each direction. Mesh 3 is similarly 8 ($2 \times 2 \times 2$) times finer than Mesh 2. There are a total of 30,520 elements in Mesh 1, 167,138 in Mesh 2, and 947,584 in Mesh 3.

Because of the finer grids in Meshes 2 and 3 and the associated computational expense, the simulations using these meshes were performed for a smaller number of time steps than for Mesh 1, and the results from the three meshes compared. The trends of variation in the difference between the results obtained using these meshes were used to estimate the mesh-independence of steady-state results.

The flow rate obtained from Mesh 1 is 71% higher than that obtained from Mesh 2 at the largest time considered in Figure 6a ($t = 1.60 \times 10^{-5}$ s), while that from Mesh 2 is 8.5% higher than that from Mesh 3. At the larger times considered in Figure 6b, the difference in flow rate between Mesh 1 and Mesh 2 drops to 22% at the largest time shown ($t = 1.13 \times 10^{-4}$ s). Since the error in using the coarser meshes reduces as steady state is approached, it is expected that the flow rates at steady state obtained from Mesh 1 would deviate from mesh-independent results by no greater than 20%.

The net flow rate at zero back pressure obtained from the vibrating diaphragm acting alone (with no EHD) for Mesh 1 is plotted in Figure 7a. Almost no difference was found in the

results obtained from Mesh 1 and Mesh 2 (and the latter are not shown). Similarly, the net flow rate at zero back pressure obtained from the combined action of both the vibrating diaphragm and EHD using Mesh 1 and Mesh 2 is compared in Figure 7b. These results are within 22% for the largest time considered.

Case 1 ($a_c = 1 \text{ mm}$, $n_{elec} = spac_{elec} = 10 \text{ }\mu\text{m}$)

The flow rate obtained from EHD action only using Mesh 1 is plotted in Figure 8a as a function of time, till the flow reaches almost steady-state behavior at a flow rate of $Q = 3.72 \times 10^{-10} \text{ m}^3 / \text{sec}$. The net flow rate at zero back pressure obtained from the combined action of both the vibrating diaphragm and EHD is shown in Figure 8b. The net flow rate is plotted as a function of time till the results reach a quasi-steady state where the variation in the flow rate is due to the action of the vibrating diaphragm only.

The net flow rate obtained from the vibrating diaphragm acting alone (with no EHD, Figure 7a) shows that the nozzle-diffuser pump does not always create a net flow in the positive direction, contrary to what might be expected. This is believed to be due to the small amplitude of diaphragm vibration, which leads to relatively small fluid velocities. The direction-dependence of flow through nozzle-diffuser elements is significant only at high velocities because it depends on the extent of momentum transferred [14,51]. At smaller velocities the kinetic energy of the fluid is small compared to the pressure energy because of significant viscous losses. The time-averaged flow rate for the present case is still in the forward direction, with $Q = 1.37 \times 10^{-14} \text{ m}^3 / \text{sec}$. It may be noted that this is four orders of magnitude smaller than the flow rate obtained from EHD action alone.

Flow rates from the outlet of the pump due to the action of the vibrating diaphragm only, EHD only and the combined action of both the vibrating diaphragm and EHD are shown in Figure 9. It is seen that even though the net flow because of EHD is much larger than that due to

the vibrating diaphragm, the absolute (transient) magnitude of flow caused by the vibrating diaphragm action is much larger than that of the EHD. Also, flow due to the combined action of the vibrating diaphragm and EHD is roughly equal to the sum of flows from their action independent of each other.

Case 2 ($a_c = 2 \text{ mm}$, $n_{elec} = spac_{elec} = 10 \text{ }\mu\text{m}$)

A pump with vibrating diaphragm diameter of 2 mm and with the rest of the dimensions being the same as the pump in Case 1 above is simulated. The vibrating diaphragm in this pump is expected to create higher flow rates and hence higher flow rectification. This would also cause higher net flow rates due to the action of the vibrating diaphragm alone. A mesh similar to Mesh 1 was used. It had same number of elements in the nozzle-diffuser and inlet-outlet chambers, while the number of nodes in the pumping chamber was increased such that the size of the smallest element and grading level remained the same as for Case 1. There were 26 elements at the widest point of the pumping chamber and 94 along its length for a total of 43,356 elements in the model.

The net flow due to the combined action of the vibrating diaphragm and EHD and that due to their independent action for this case is plotted in Figure 10. The sum of net flows from independent actions of the vibrating diaphragm and EHD is smaller than that obtained with their combined action. This is due to an increase in efficiency of induction EHD action due to the very high flow rates created by vibrating diaphragm. This phenomenon of increased efficiency under high bulk velocity has been explored in detail in [52]. This effect would be further amplified as the size of the diaphragm is increased.

Case 3 ($a_c = 1 \text{ mm}$, $n_{elec} = spac_{elec} = 5 \text{ }\mu\text{m}$)

The effect of electrode width and electrode spacing on flow due to EHD was studied with this case. The electrode width and spacing of 10 μm considered in Case 1 were reduced to 5 μm

in this case, with all other parameters remaining unchanged. The flow rate at zero back pressure obtained from this pump design is compared to that in Case 1 for EHD action only in Figure 11. Mesh 2 was used in this case, as this corresponds to each electrode being represented by one element in the mesh (leading to the same electrode mesh density as in Mesh 1 for Case 1).

The flow rate due to EHD action only at the highest time in Figure 11 for this pump is 56% higher than that for the original pump in Case 1. Since the charge relaxation time is not affected by variation of wavelength of the potential wave, induction of charges is expected to follow the same temporal variation as for the pump in Case 1. Further, since the potential wave frequency for the two cases is the same, the time variation of Coulomb forces and hence that of the flow is expected to be similar.

The simulation results presented above are for water doped with KCl. Use of deionized water instead would lead to much lower flow rates, because the electrical conductivity gradient is not as high for undoped water. However, addition of salt can cause corrosion of metals coming into contact with the liquid. An alternative working fluid is the Fluorinert FC-75, which in addition to being non-corrosive is also a dielectric. The relative performance of FC-75 in terms of flow rate as compared to the salt solution considered in the present work can be estimated using a simplified form of Eq. (15). For $\eta \ll 2kd \ll 1$, it reduces to $v_x = \left[-\eta S \epsilon k V^2 / 12 (1+S)^2 \mu_{visc} \right] (\zeta - \zeta^3)$. Hence for a pump of a given geometry, potential wave voltage and amplitude, operating at the optimal frequency (corresponding to $S = 1$), $v_x \propto \eta \epsilon / \mu_{visc} = \sigma_1 \epsilon / \sigma_0 \mu_{visc}$. The fluid velocity due to induction EHD for the two fluids can be compared using this expression.

The variation of electrical conductivity of FC-75 with temperature is given by $\sigma = 2.672 \times 10^{-12} \exp(-991.3/T)$ [38]. The kinematic viscosity and the density of FC-75 at 25°C

is 0.8 cSt and 1770 kg/m³, respectively [53]. The dielectric constant of FC-75 is 1.86 at 1 kHz such that $\epsilon = 1.65 \times 10^{-11}$ F/m. Hence, the ratio of $\sigma_1 \epsilon / \sigma_0 \mu_{visc}$ for the two fluids for the same temperature difference is $(\sigma_1 \epsilon / \sigma_0 \mu_{visc})_{FC-75} / (\sigma_1 \epsilon / \sigma_0 \mu_{visc})_{Water-KCl} = 6.5 \times 10^{-3}$. The flow rate achieved with FC-75 would thus be 0.65% that obtained for the salt solution. However, this flow rate can be increased by increasing the electrical conductivity gradient or permittivity. The electrical conductivity gradient can be increased by adding antistatic additives [38]. Other fluids for use in conjunction with induction EHD have been studied [23,29,38,54,55]. Also, even though the flow rate from a single micropump can be low, a large number of such micropumps could be used in series and parallel in an integrated microchannel cooling system, leading to significant flow rates in an integrated cooling system.

The maximum enhancement in flow rate due to the increase in efficiency of induction EHD obtained in the present work is 150%. This can be increased significantly by optimizing the pump design (size, geometry and diaphragm frequency). An increase of greater than ninety-fold in efficiency was observed for a similar repulsion-type induction EHD pump due to an external pressure gradient [52]. It should be noted that although the action of the vibrating diaphragm causes only a small net flow rate, it increases the local velocity of the fluid by several orders of magnitude and hence the heat transfer coefficient, which depends on the local velocity, is significantly higher than would be expected for a flow of this bulk velocity.

CONCLUSIONS

The preliminary design of a micropump for an integrated microchannel cooling system is presented. A comprehensive numerical model of the micropump is developed and validated. A force density approach is used to model induction EHD. The model can predict transient variation in charge density as well as the effect of different voltage profiles on charge induction

and the resultant flow. The flow rate achieved from the pump, as well as the effects of various parameters on the flow rate, are predicted.

A steady-state flow rate of approximately $3.7 \times 10^{-10} \text{ m}^3/\text{sec}$ ($= 22.2 \text{ } \mu\text{l}/\text{min}$) is predicted for a micropump with a 1 mm diameter diaphragm. The electrode width and spacing is $10 \text{ } \mu\text{m}$ each and the overall dimensions of this pump are $1.5 \text{ mm} \times 1 \text{ mm}$. A decrease in the electrode width and spacing to $5 \text{ } \mu\text{m}$ each, causes the flow to increase to approximately $33 \text{ } \mu\text{l}/\text{min}$. For a pump with a diaphragm of diameter 2 mm and electrode width and spacing of $10 \text{ } \mu\text{m}$ each, a flow rate of approximately $50 \text{ } \mu\text{l}/\text{min}$ is predicted. Further optimization of different pump parameters is expected to increase the flow rate significantly.

The flow rectification in a nozzle-diffuser micropump was found to be higher for large diaphragms. Also, for large diaphragms the flow achieved from the combined action of the vibrating diaphragm and EHD in the micropump was larger than the sum of the flows obtained from their action independent of each other, while there was little difference for pumps with smaller diaphragms.

REFERENCES

- [1] Thermal management technology roadmap of the *National Electronics Manufacturing Initiative* (NEMI), 2002.
- [2] Jiang, L., Mikkelsen, J., Koo, J.M., Huber, D., Yao, S., Zhang, L., Zhou, P., Maveety, J.G., Prasher, R., Santiago, J.G., Kenny, T.W., Goodson, K.E., 2002, "Closed-loop electroosmotic microchannel cooling system for VLSI circuits," *IEEE Transactions on Components and Packaging Technologies*, **25**, pp. 347-355.
- [3] Darabi, J., Ohadi, M. M., and DeVoe, D., 2001, "An electrohydrodynamic polarization micropump for electronic cooling," *Journal of Microelectromechanical Systems*, **10**, pp. 98-106.
- [4] Wong, C. C., Adkins, D. R., and Chu, D., 1996, "Development of a micropump for microelectronic cooling," *Microelectromechanical Systems (MEMS)*, DSC **59**, pp. 239-244.
- [5] Singhal, V., Garimella, S. V., and Raman, A., 2004, "Microscale pumping technologies for microchannel cooling systems," *Applied Mechanics Reviews*, **57**, pp. 191-221.

- [6] Stemme, E., and Stemme, G., 1993, "A valveless diffuser/nozzle-based fluid pump," *Sensors and Actuators A: Physical*, **39**, pp. 159-167.
- [7] Gerlach, T., Schuenemann, M., and Wurmus, H., 1995, "A new micropump principle of the reciprocating type using pyramidic micro flowchannels as passive valves," *Journal of Micromechanics and Microengineering*, **5**, pp. 199-201.
- [8] Forster, F.K., Bardell, R.L., Afromowitz, M.A., Sharma, N.R., and Blanchard, A., 1995, "Design, fabrication and testing of fixed-valve micro-pumps," *Proceedings of the ASME Fluids Engineering Division*, FED **234**, pp. 39-44.
- [9] Jiang, X. N., Zhou, Z. Y., Huang, X. Y., Li, Y., Yang, Y., and Liu, C. Y., 1998, "Micronozzle/diffuser flow and its application in micro valveless pumps," *Sensors and Actuators A: Physical*, **70**, pp. 81-87.
- [10] Jeong, O. C., and Yang, S. S., 2000, "Fabrication and test of a thermopneumatic micropump with a corrugated p+ diaphragm," *Sensors and Actuators A: Physical*, **83**, pp. 249-255.
- [11] Olsson, A., Stemme, G., and Stemme, E., 1995, "A valve-less planar fluid pump with two pump chambers," *Sensors and Actuators A: Physical*, **47**, pp. 549-556.
- [12] Olsson, A., Enoksson, P., Stemme, G., and Stemme, E., 1997, "Micromachined flat-walled valveless diffuser pumps," *Journal of Microelectromechanical Systems*, **6**, pp. 161-166.
- [13] Gerlach, T., and Wurmus, H., 1995, "Working principle and performance of the dynamic micropump," *Sensors and Actuators A: Physical*, **50**, pp. 135-140.
- [14] Singhal, V., Garimella, S. V., and Murthy, J., 2004, "Low Reynolds Number Flow through Nozzle-Diffuser Elements in Valveless Micropumps," *Sensors and Actuators A: Physical*, **113**, pp. 226-235.
- [15] Chattock, A., 1899, "On the velocity and mass of ions in the electric wind in air," *Philosophical Magazine*, London, England, **48**, pp. 401-420.
- [16] Stuetzer, O., 1959, "Ion drag pressure generation," *Journal of Applied Physics*, **30**, pp. 984-994.
- [17] Richter, A., Plettner, A., Hofmann, K. A., and Sandmaier, H., 1991, "A micromachined electrohydrodynamic (EHD) pump," *Sensors and Actuators A: Physical*, **29**, pp. 159-168.
- [18] Ahn, S.-H., and Kim, Y.-K., 1998, "Fabrication and experiment of a planar micro ion drag pump," *Sensors and Actuators A: Physical*, **70**, pp. 1-5.
- [19] Schlitz, D. J., Garimella, S. V., and Fisher, T. S., 2003, "Numerical simulation of microscale ion driven air flow," *ASME International Mechanical Engineering Congress and Exposition*, Washington, D.C., IMECE2003-41316.
- [20] Manz, A., Effenhauser, C. S., Burggraf, N., Harrison, D. J., Seiler, K., and Fluri, K., 1994, "Electroosmotic pumping and electrophoretic separations for miniaturized chemical analysis systems," *Journal of Micromechanics and Microengineering*, **4**, pp. 257-265.
- [21] Zeng, S., Chen, C. H., Mikkelsen, Jr., J. C., and Santiago, J. C., 2001, "Fabrication and characterization of electroosmotic micropumps," *Sensors and Actuators B: Chemical*, **79**, pp. 107-114.

- [22] Melcher, J. R., 1966, "Traveling-wave induced electroconvection," *The Physics of Fluids*, **10**, pp. 1548-1555.
- [23] Melcher, J. R., and Firebaugh, M. S., 1967, "Traveling-wave bulk electroconvection induced across a temperature gradient," *The Physics of Fluids*, **10**, pp. 1178-1185.
- [24] Melcher, J. R., 1981, *Continuum Electromechanics*, MIT Press, Cambridge, MA.
- [25] Seyed-Yagoobi, J., Chato, J.C., Crowley, J.M., and Krein, P.T., 1989, "Induction electrohydrodynamic pump in vertical configuration, Part 1 - Theory," *ASME Journal of Heat Transfer*, **111**, pp. 664-669.
- [26] Wawzyniak, M., Seyed-Yagoobi, J., and Morrison, G. L., 2000, "An experimental study of electrohydrodynamic induction pumping of a stratified liquid/vapor medium," *ASME Journal of Heat Transfer*, **122**, pp. 200-203.
- [27] Gerdt, R. E., Crowley, J. M., and Chato, J. C., 1978, "Electrohydrodynamic pumping of cable oil," *Journal of Electrostatics*, **5**, pp. 477-488.
- [28] Kuo, B. S., Chato, J. C., and Crowley, J. M., 1984, "A finite element model for temperature induced electrohydrodynamic pumping in horizontal pipes," *ASME Journal of Heat Transfer*, **106**, pp. 78-84.
- [29] Seyed-Yagoobi, J., Chato, J.C., Crowley, J.M., and Krein, P.T., 1989, "Induction electrohydrodynamic pump in vertical configuration, Part 2 - Experimental Study," *ASME Journal of Heat Transfer*, **111**, pp. 670-674.
- [30] Seyed-Yagoobi, J., 1990, "A theoretical study of induction electrohydrodynamic pumping in outer space," *ASME Journal of Heat Transfer*, **112**, pp. 1095-1097.
- [31] Haller, K., and Moesner, F., 1998, "Theoretical considerations on the electrohydrodynamic propulsion," *Proceedings of 4th International Conference on Motion and Vibration Control MOVIC'98*, Zurich, pp. 1121-1126.
- [32] Crowley, J. M., 1980, "The efficiency of electrohydrodynamic pumps in the attraction mode," *Journal of Electrostatics*, **8**, pp. 171-181.
- [33] Bart, S. F., Tavrow, L. S., Mehregany, M., and Lang, J. H., 1990, "Microfabricated electrohydrodynamic pumps," *Sensors and Actuators A: Physical*, **21-23**, pp. 193-197.
- [34] Fuhr, G., Hagedorn, R., Muller, T., Benecke, W., and Wagner, B., 1992, "Microfabricated electrohydrodynamic (EHD) pumps for liquids of higher conductivity," *Journal of Microelectromechanical Systems*, **1**, pp. 141-146.
- [35] Fuhr, G., Schnelle, T., and Wagner, B., 1994, "Travelling wave-driven microfabricated electrohydrodynamic pumps for liquids," *Journal of Micromechanics and Microengineering*, **4**, pp. 217-226.
- [36] Moesner, F. M., and Higuchi, T., 1995, "Devices for particle handling by an AC electric field," *Proceedings of IEEE Micro Electro Mechanical Systems*, pp. 66-71.
- [37] Kashani, R., Kang, S., and Hallinan, K P., 2000, "Micro-scale electrohydrodynamic pumped high performance actuation," *Journal of Intelligent Material Systems & Structures*, **11**, pp 343-350.

- [38] Bohinsky, B. J., and Seyed-Yagoobi, J., 1990, "Induction electrohydrodynamic pumping-selecting an optimum working fluid," *Proceedings of the IEEE-IAS-1990 Annual Meeting*, Seattle, Washington, pp.795-801.
- [39] Margo, B. D., and Seyed-Yagoobi, J., 1993, "Heat transfer enhancement resulting from induction electrohydrodynamic pumping of a single phase liquid," *ASHRAE Transactions*, **99**, pp. 1217-1224.
- [40] Margo, B. D., and Seyed-Yagoobi, J., 1994, "Heat transfer enhancement under various orientations resulting from attraction mode induction electrohydrodynamic pumping," *ASME Journal of Heat Transfer*, **116**, pp. 598-603.
- [41] Seyed-Yagoobi, J., Margo, B. D., and Bryan, J. E., 1994, "Effect of frequency on heat transfer enhancement in temperature induced electrohydrodynamic pumping," *IEEE Transactions on Dielectrics and Electrical Insulation*, **1**, pp. 468-473.
- [42] Wawzyniak, M., and Seyed-Yagoobi, J., 2001, "Electrohydrodynamic induction pumping of a stratified liquid/vapor medium in the presence of volumetric and interface electric charges," *IEEE Transactions on Industry Applications*, **37**, pp. 950-958.
- [43] Brand, K., and Seyed-Yagoobi, J., 2002, "Effect of electrode position on electrohydrodynamic induction pumping of a stratified liquid/vapor medium," *IEEE Transactions on Industry Applications*, **38**, pp. 389-400.
- [44] Singhal, V., and Garimella, S. V., "A novel micropump for electronics cooling," *International Mechanical Engineering Congress and Exposition, IMECE2004-61147*, Anaheim, CA, 2004.
- [45] Seyed-Yagoobi, J., Bryan, J. and Castaneda, J., 1995, "Theoretical analysis of ion-drag pumping," *IEEE Transactions on Industry Applications*, **31**, pp. 469-476.
- [46] FIDAP 8.7.2, FIDAP User's Manual, Fluent Inc, Lebanon, NH, 2003.
- [47] GAMBIT 2.0.0, Gambit 2.0 User's Guide, Fluent Inc, Lebanon, NH, 2003.
- [48] Kim, J., and Xu, X., "Laser-based fabrication of polymer micro-pump," *Journal of Microlithography, Microfabrication, and Microsystems*, **3**, No. 1, pp. 152-158.
- [49] FLUENT 6.0, Fluent 6.0 User's Guide, Fluent Inc, Lebanon, NH, 2003.
- [50] Incropera, F. P., and Dewitt, D. P., 1998, *Fundamentals of Heat and Mass Transfer*, John Wiley & Sons, New York.
- [51] Gerlach, T., 1998, "Microdiffusers as dynamic passive valves for micropump applications," *Sensors and Actuators A: Physical*, **69**, pp.181-191.
- [52] Singhal, V., and Garimella, S. V., "Influence of bulk fluid velocity on efficiency of electrohydrodynamic pumping," *Journal of Fluids Engineering* (in review).
- [53] 3M Specialty Materials, Fluorinert Liquids Product Manual, St. Paul, MN, 1999.
- [54] Washabaugh, A. P., Zahn, M., and Melcher, J. R., 1989, "Electrohydrodynamic traveling-wave pumping of homogeneous semi-insulating liquids," *IEEE Transactions on Electrical Insulation*, **24**, pp. 807-834.

[55] Castaneda, J.A., and Seyed-Yagoobi, J., 1991, "Electrohydrodynamic pumping of refrigerant 11," *Proceedings of the IEEE-IAS Annual Meeting*, Dearborn, Michigan, pp. 500-503.

LIST OF TABLES

Table 1. Comparison of predicted flow rates from present model to numerical and experimental results from [48].

Table 2. Dimensions and pump parameters of the three pump designs considered.

Table 3. Properties of the working fluid (water doped with KCl).

LIST OF FIGURES

Figure 1. (a) Top view, and (b) Side view of new micropump design.

Figure 2. Flow rectification in a valveless micropump: (a) Expansion mode, and (b) Contraction mode. Thicker arrows imply higher volume flow rates.

Figure 3. Graphical representation of induced charges due to (a) attraction-type and (b) repulsion-type induction EHD. The different shading of electrodes represents the value of potential, while the number of charges corresponds to the value of charge density.

Figure 4. Geometry of the micropump considered: (a) top view of the geometry modeled, and (b) isometric view of the pump with mesh shown at the bottom surface.

Figure 5. (a) Geometry modeled for charge induction model validation; (b) Comparison of velocity profile obtained from the present numerical model to that from the analysis in [23] (y is the distance from the plate at the lower temperature).

Figure 6. Flow rate at zero back pressure from EHD only for Case 1 obtained from (a) all three meshes, and (b) for Mesh 1 and Mesh 2 over a longer time period.

Figure 7. Net flow rate at zero back pressure for Case 1 from (a) action of vibrating diaphragm only, and (b) combined action of vibrating diaphragm and EHD.

Figure 8. Flow rate at zero backpressure for Case 1 from Mesh 1 due to (a) EHD only, and (b) combined action of vibrating diaphragm and EHD.

Figure 9. Outlet flow near steady state for Case 1 due to vibrating diaphragm action only, EHD only and combined action of vibrating diaphragm and EHD.

Figure 10. Net flow rate for Case 2 obtained from the combined action of the vibrating diaphragm and EHD, as well as their action independent of each other.

Figure 11. Comparison of predicted flow rate due to EHD only from pumps in Case 1 and Case 3.

Table 1. Comparison of predicted flow rates from present model to numerical and experimental results from [48].

Source	Flow rate at zero back pressure
Experimental measurement [48] (with inlet and outlet chambers)	0.97 mm ³ /s
Numerical results [48] (without inlet and outlet chambers)	2.67 mm ³ /s
Present numerical results without inlet and outlet chambers	2.80 mm ³ /s
Present numerical results with inlet and outlet chambers	0.623 mm ³ /s

Table 2. Dimensions and pump parameters of the three pump designs considered.

Parameter	Case 1	Case 2	Case 3
Vibrating Diaphragm			
a_c (μm)	1000	2000	1000
h (μm)	50	50	50
A_{vib} (μm)	0.1	0.1	0.1
f_{vib} (kHz)	100	100	100
Nozzle-Diffuser Elements			
l_{nd} (μm)	250	250	250
n_{nd} (μm)	100	100	100
Θ	5	5	5
Inlet and Outlet Chambers			
l_{io} (μm)	200	200	200
n_{io} (μm)	500	500	500
Potential Wave			
A_p (V)	200	200	200
f_p (kHz)	122	122	122
Electrodes			
n_{elec} (μm)	10	10	5
$spac_{elec}$ (μm)	10	10	5

Table 3. Properties of the working fluid (water doped with KCl).

Property	Value
ρ	987.17 kg/m ³ [50]
μ_{vis}	0.528×10^{-3} Ns/m ² [50]
ε	7.08×10^{-10} F/m [35]
σ	0.20×10^{-3} S/m @ T = 0°C [35]
	0.70×10^{-3} S/m @ T = 72.80°C [35]

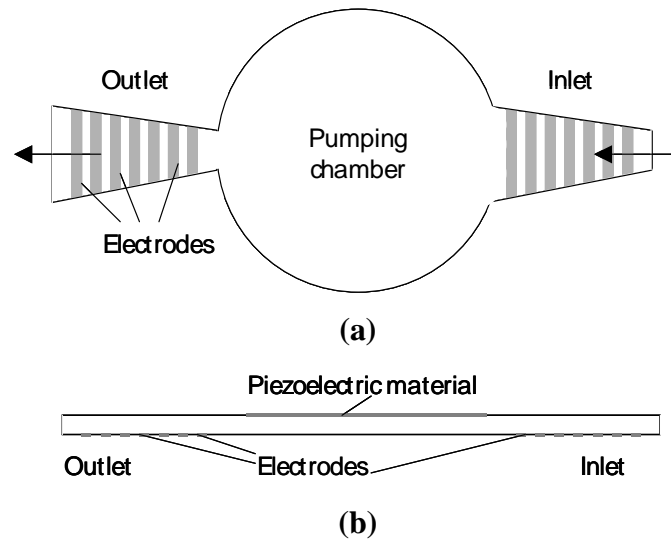


Figure 1. (a) Top view, and (b) Side view of new micropump design.

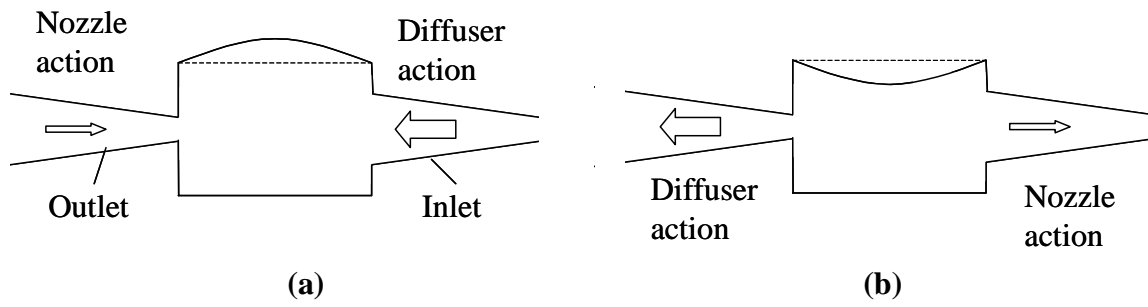
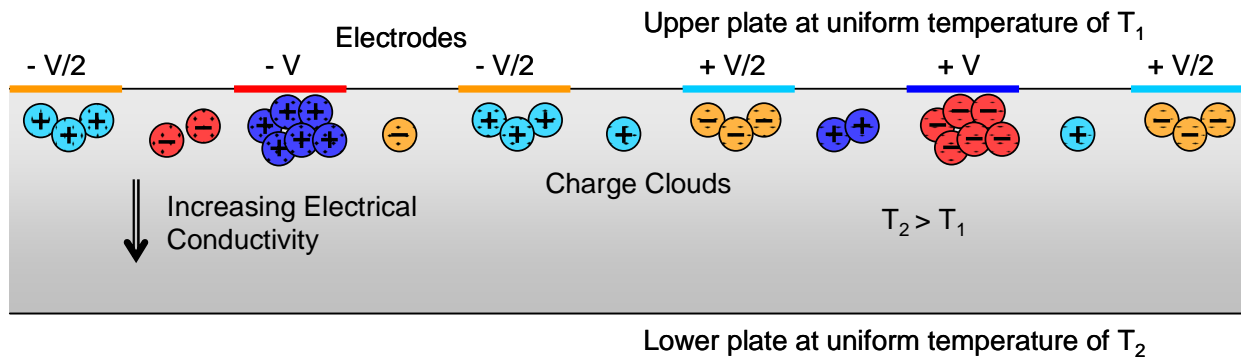
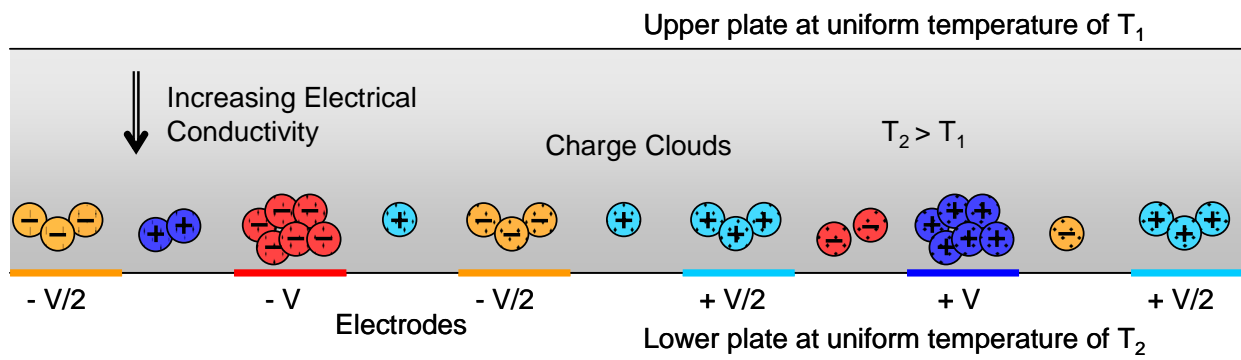


Figure 2. Flow rectification in a valveless micropump: (a) Expansion mode, and (b) Contraction mode. Thicker arrows imply higher volume flow rates.

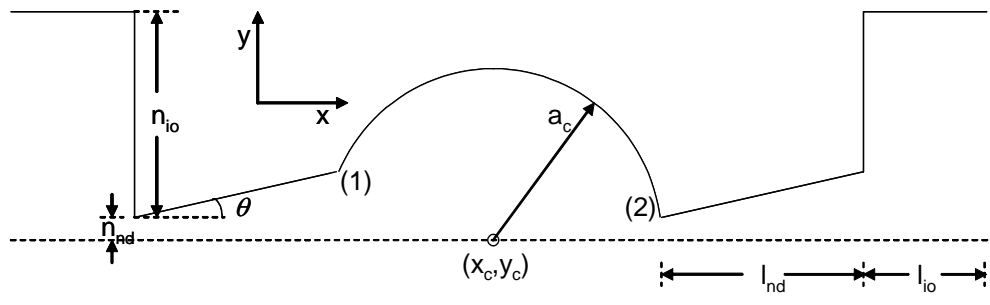


(a)

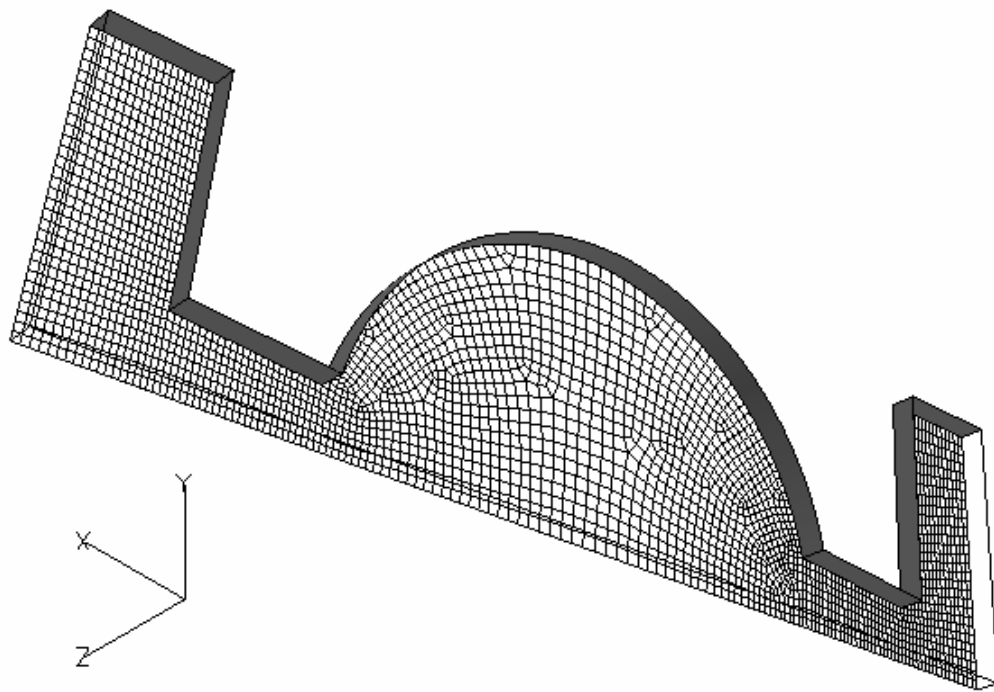


(b)

Figure 3. Graphical representation of induced charges due to (a) attraction-type and (b) repulsion-type induction EHD. The different shading of electrodes represents the value of potential, while the number of charges corresponds to the value of charge density.

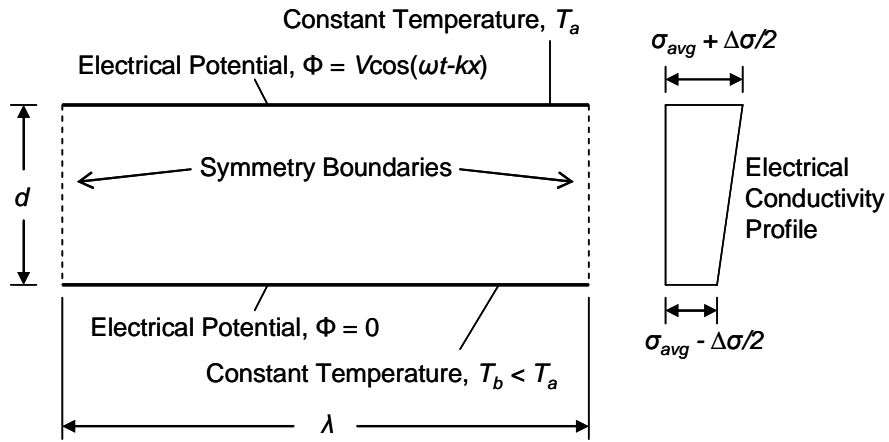


(a)

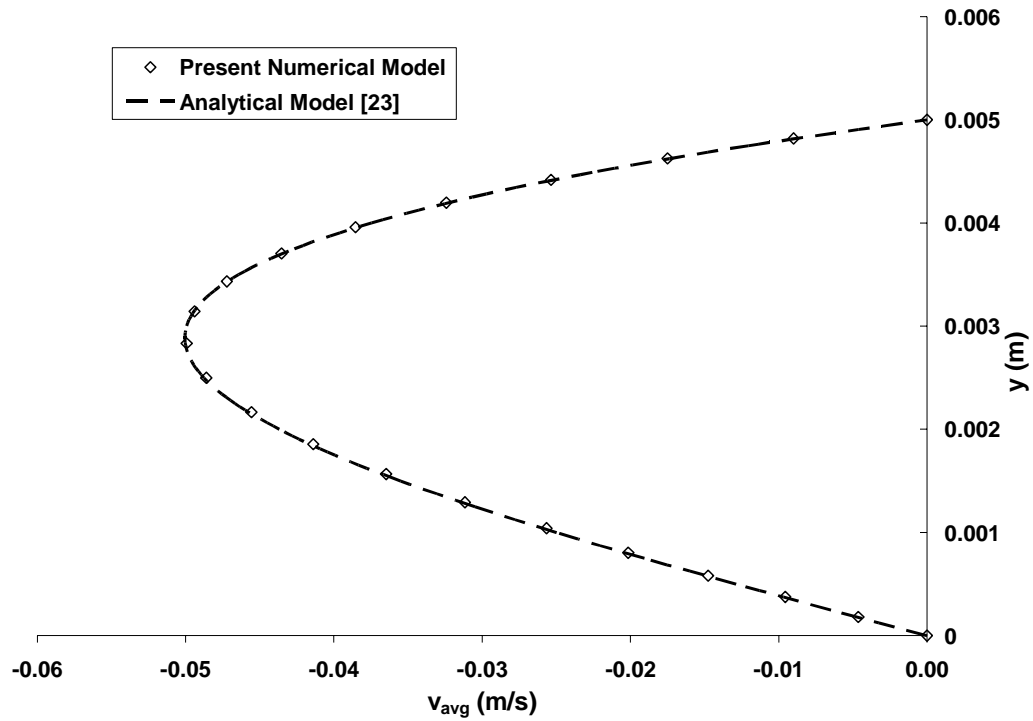


(b)

Figure 4. Geometry of the micropump considered: (a) top view of the geometry modeled, and (b) isometric view of the pump with mesh shown at the bottom surface.

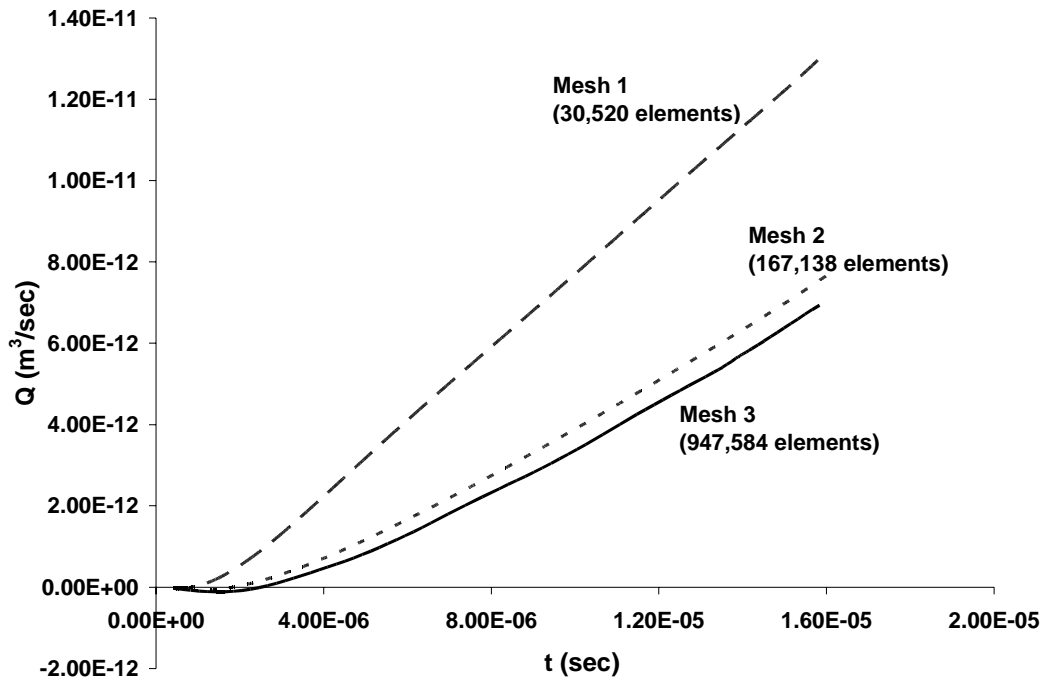


(a)

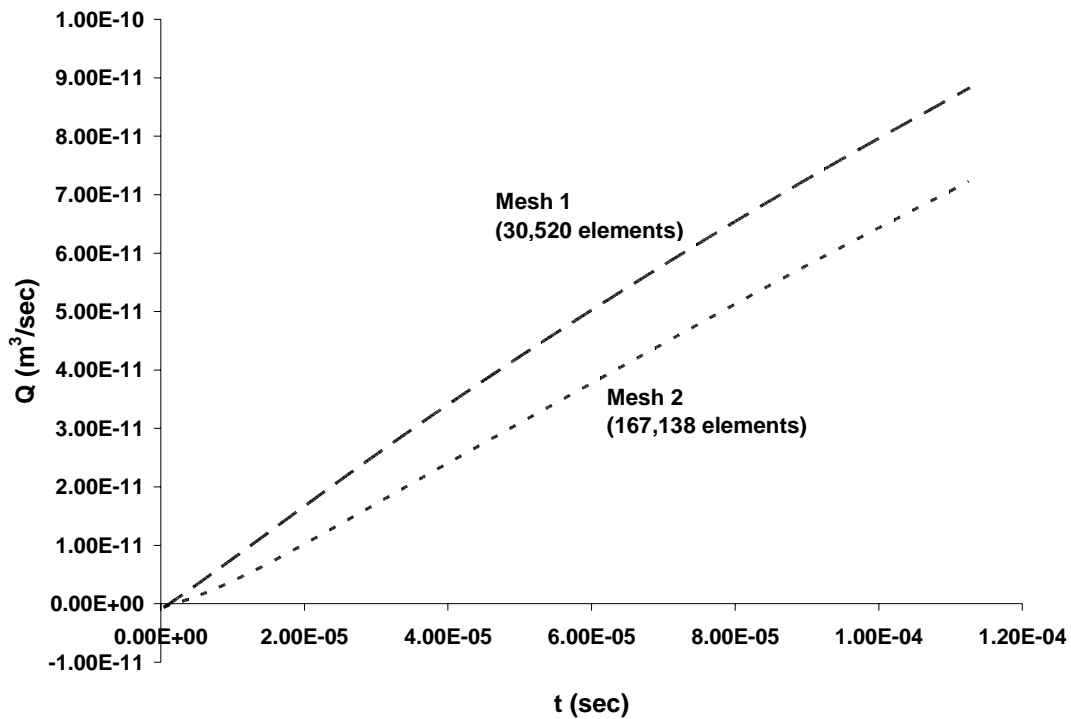


(b)

Figure 5. (a) Geometry modeled for charge induction model validation; (b) Comparison of velocity profile obtained from the present numerical model to that from the analysis in [23] (y is the distance from the plate at the lower temperature).

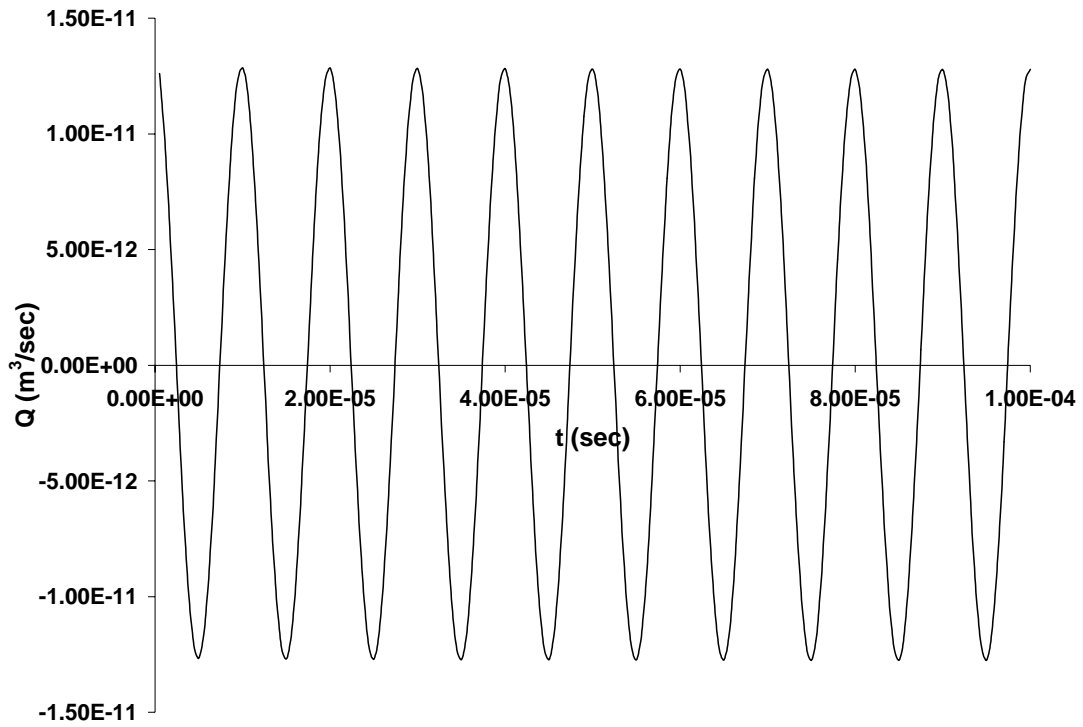


(a)

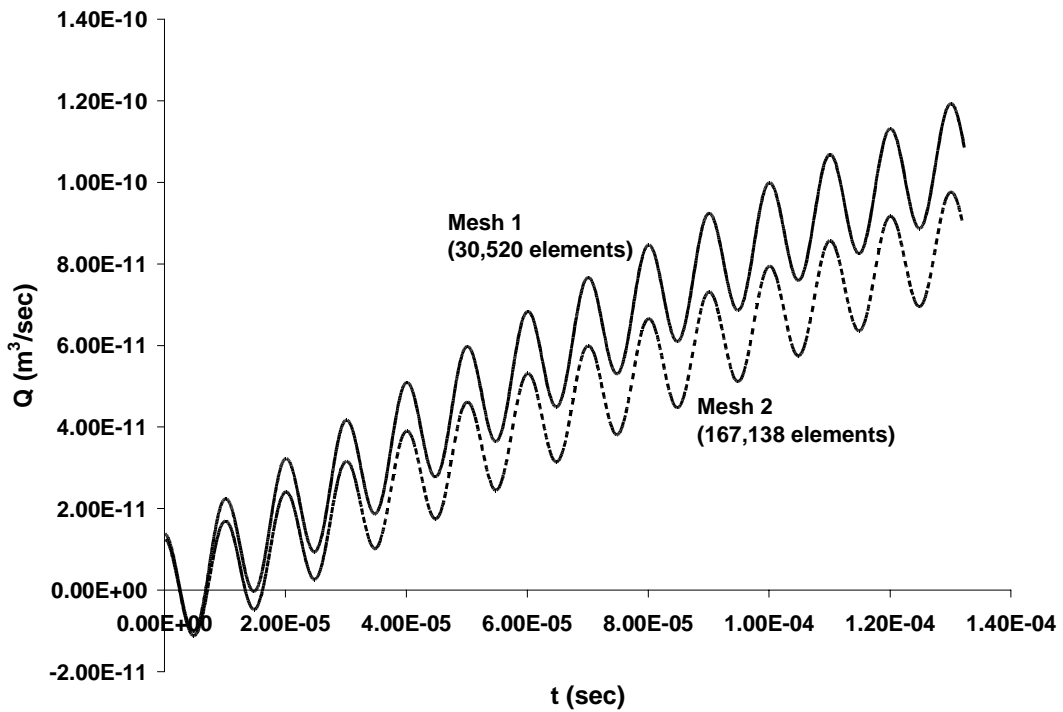


(b)

Figure 6. Flow rate at zero back pressure from EHD only for Case 1 obtained from (a) all three meshes, and (b) for Mesh 1 and Mesh 2 over a longer time period.

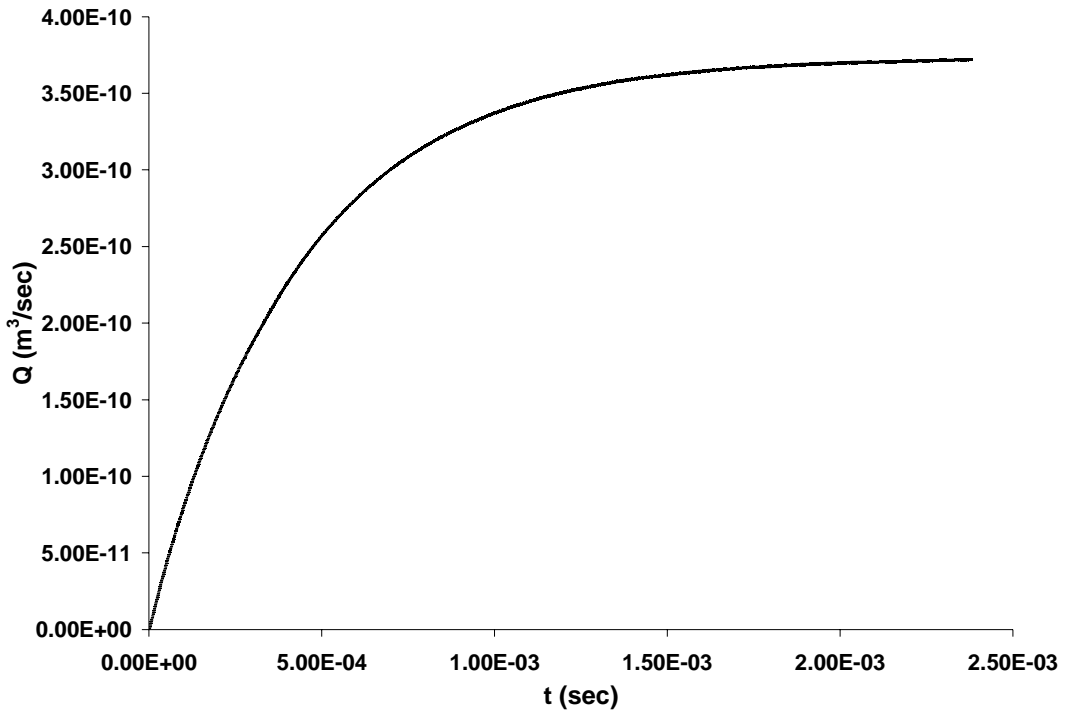


(a)

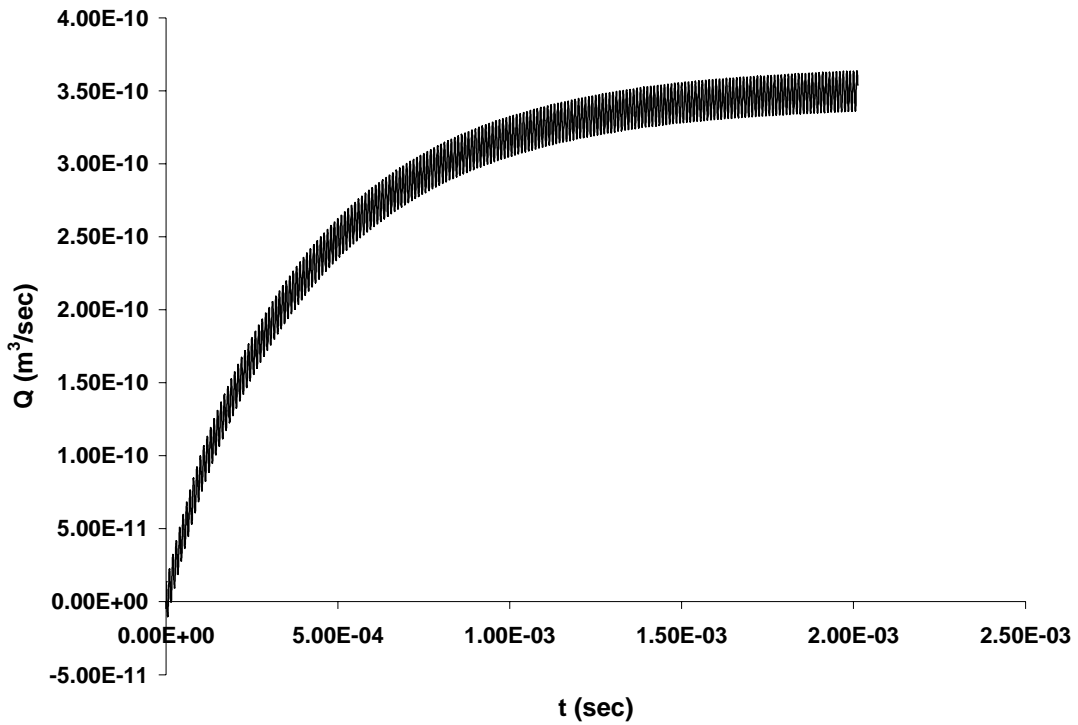


(b)

Figure 7. Net flow rate at zero back pressure for Case 1 from (a) action of vibrating diaphragm only, and (b) combined action of vibrating diaphragm and EHD.



(a)



(b)

Figure 8. Flow rate at zero backpressure for Case 1 from Mesh 1 due to (a) EHD only, and (b) combined action of vibrating diaphragm and EHD.

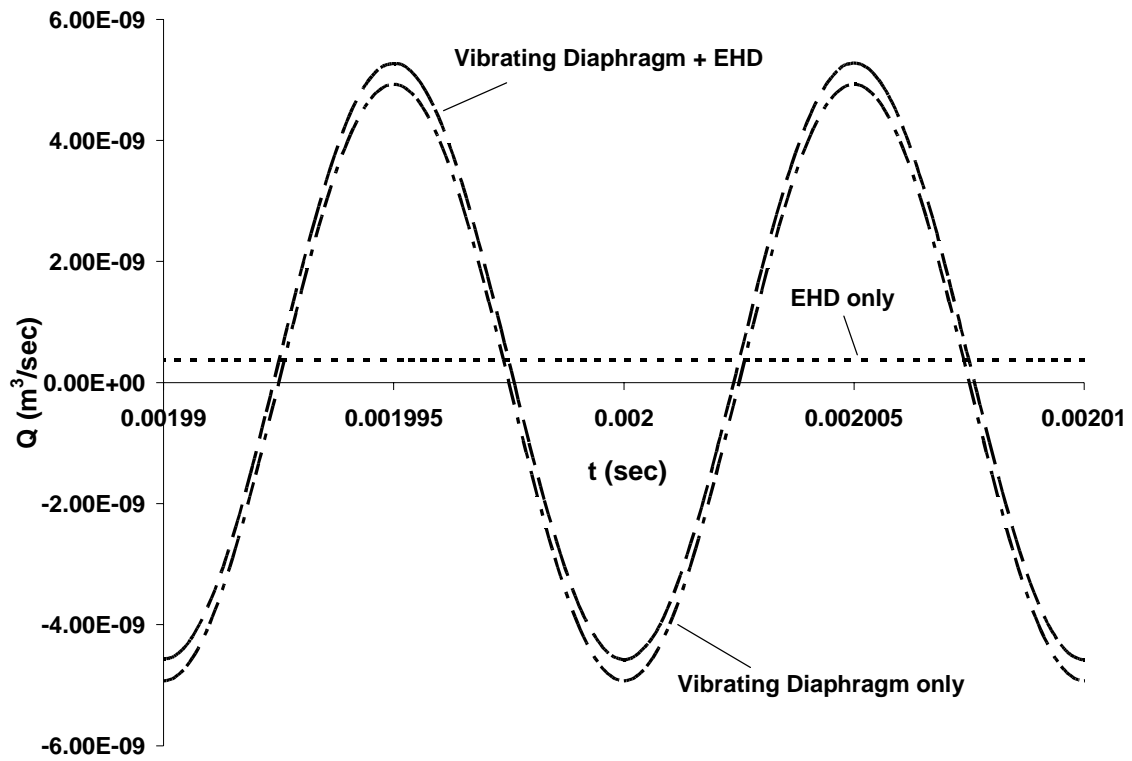


Figure 9. Outlet flow near steady state for Case 1 due to vibrating diaphragm action only, EHD only and combined action of vibrating diaphragm and EHD.

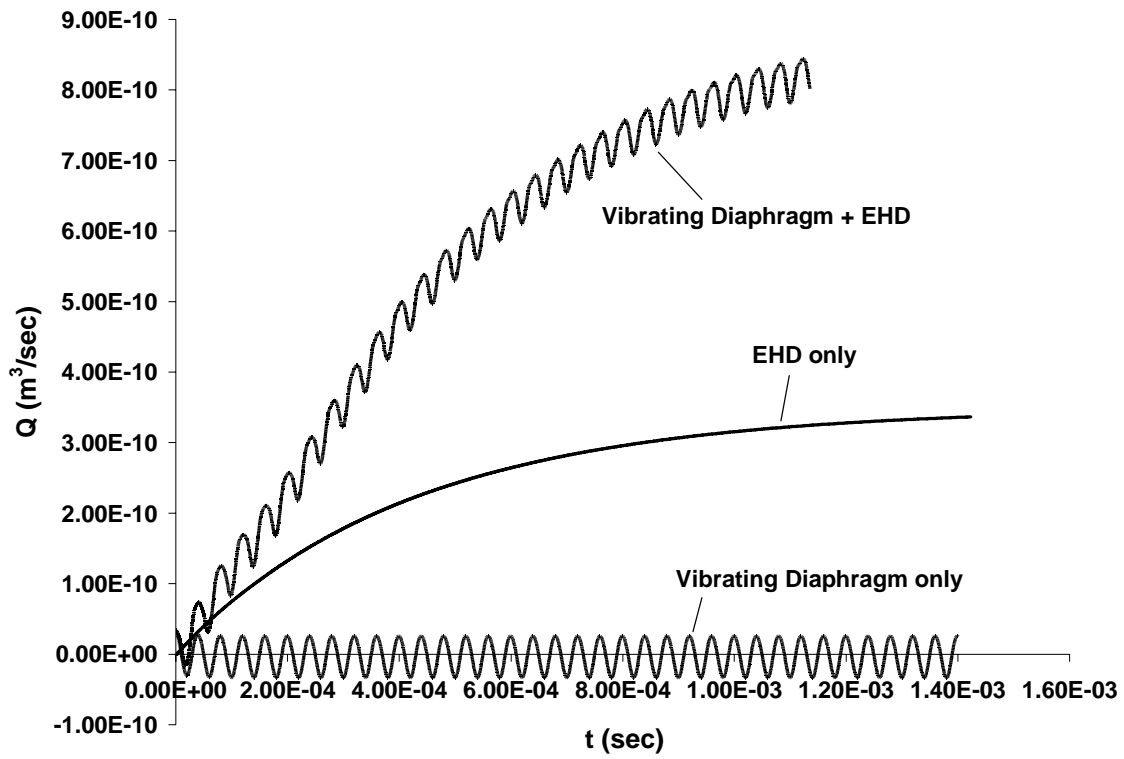


Figure 10. Net flow rate for Case 2 obtained from the combined action of the vibrating diaphragm and EHD, as well as their action independent of each other.

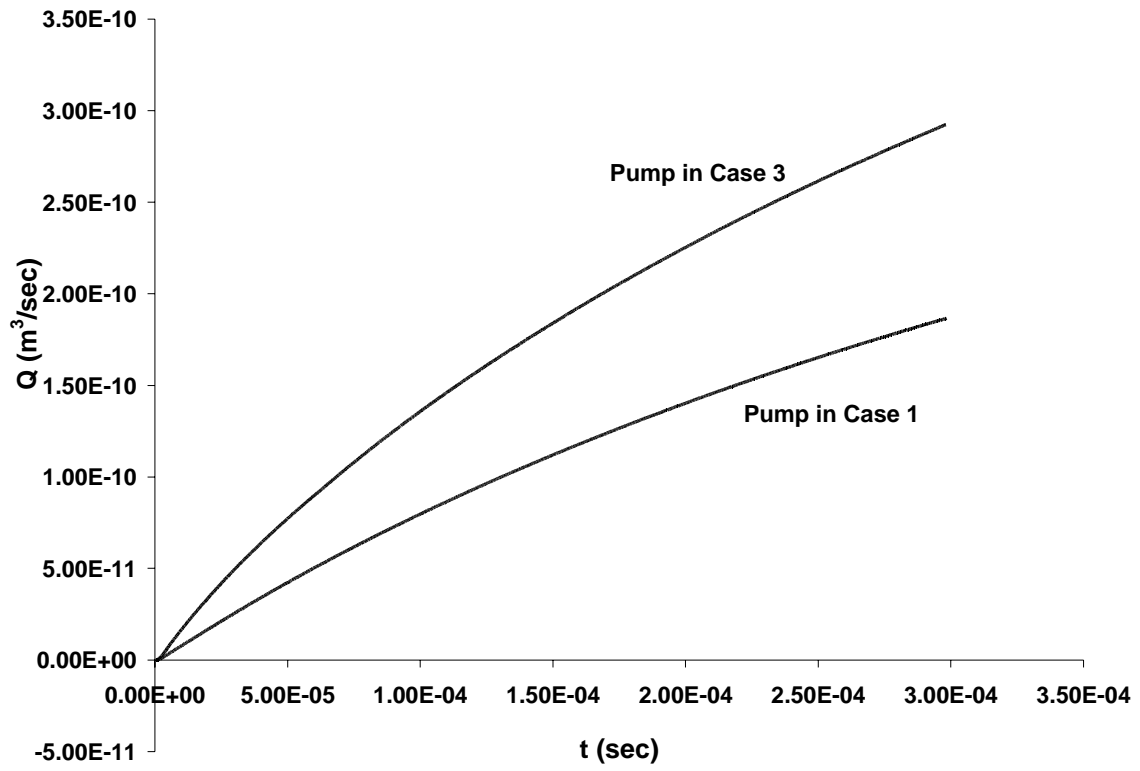


Figure 11. Comparison of predicted flow rate due to EHD only from pumps in Case 1 and Case 3.